



ELSEVIER

Journal of Crystal Growth 154 (1995) 386–400

JOURNAL OF **CRYSTAL  
GROWTH**

# Simulations of experimentally observed dendritic growth behavior using a phase-field model

B.T. Murray <sup>a</sup>, A.A. Wheeler <sup>b,\*</sup>, M.E. Glicksman <sup>c</sup>

<sup>a</sup> National Institute of Standards and Technology, Gaithersburg, Maryland 20899, USA

<sup>b</sup> School of Mathematics, University of Bristol, Bristol, BS8 1TW, UK

<sup>c</sup> Materials Engineering Department, Rensselaer Polytechnic Institute, Troy, New York 12180-3590, USA

Received 25 October 1994; manuscript received in final form 22 February 1995

## Abstract

An anisotropic phase-field model is used to simulate numerically dendritic solidification for a pure material in two dimensions. The phase-field model has been formulated to include the effect of four-fold anisotropy in both the surface energy and interfacial kinetics. The computations presented here are intended to model qualitatively experimentally observed dendritic solidification morphology. In particular, we simulate the growth into an under-cooled melt of two dendrite tips which have formed as the result of a splitting event. The computation exhibits the competition between the two growing dendrite branches and the eventual predominance of one branch. Also, we simulate the effect of time-periodic forcing of an isolated dendrite tip on the mechanism of sidebranch formation. Although it is not yet computationally feasible to adequately verify convergence of the phase-field solutions, the phase-field simulations presented show many of the qualitative features observed in dendritic growth experiments.

## 1. Introduction

Diffuse interface or phase-field models for the theoretical investigation of phase transitions have become the subject of considerable interest. While the fundamental ideas associated with diffuse interface theory have existed for a long time, only in the last ten years or so has substantial effort been focused on the development of diffuse interface models for first-order phase transitions

such as solidification. The classical “sharp interface” free boundary formulation models solidification of a pure material by treating the heat flow in each phase separated by a moving surface, representing the interface, upon which boundary conditions are prescribed. In contrast, the phase-field method introduces a continuous transition between the two phases across a thin layer of finite thickness. An additional variable called the phase field is introduced whose value at a point identifies the phase. The computational advantage of the phase-field approach is that the location of the phase change interface does not have to be explicitly determined. The trade-off in avoiding explicit interface tracking is the need to solve an additional field equation which has very

\* Corresponding author. Fax: +44 1703 595147.

<sup>1</sup> Permanent address: Faculty of Mathematical Studies, University of Southampton, Highfield, Southampton, SO17 1BJ, UK.

thin regions with large spatial gradients. If the computational requirements associated with solving the phase-field equation can be adequately satisfied, then it may prove to be the method best suited for the numerical simulation of phenomena with complicated morphology, such as dendritic growth; a situation which remains difficult to solve numerically employing algorithms based on the classical free boundary formulation.

The development of a field equation for an order parameter or phase-field variable that can be used to model solidification borrows ideas from the related physical problems of diffuse phase boundaries and critical point phenomena [1–3]. An early formulation of a phase-field model for first-order phase transitions was given by Langer [4], but the first published description seems to be that of Fix [5]. In a later publication of Langer [6], which discusses the phase-field idea, he attributes the use of the name “phase-field” to Fix. A diffuse interface model for solidification similar to the Langer–Fix formulation was described by Collins and Levine [7]. A significant amount of the early work on the development and analysis of a phase-field model for first-order phase transitions was done by Caginalp [8–10]. Also an important extension, the inclusion of anisotropic effects into a phase-field model, was first done by Caginalp and collaborators [11–13]. Several computations using a phase-field model have been performed for simple shapes in one or two dimensions [5,13–15]. Early dendritic computations employing a phase-field like approach were performed by Umantsev et al. [16]. The computations of Kobayashi [17] generated considerable interest in the phase-field method. He employed an anisotropic phase-field model for a pure material in two dimensions and computed the evolution of sidebranched, dendrite-like structures growing into an undercooled melt. More recently, he has extended his computations to three spatial dimensions and has simulated realistic looking dendritic structure [18]. Although questions remain concerning the behavior of phase-field models and the accuracy of particular computations, Kobayashi’s work was responsible for demonstrating the potential of the phase-field approach as a computational tool for model-

ing complicated, realistic solidification structures and for generating considerable interest in the materials science community.

The computations presented here are based on a recent phase-field model for a pure material which combines desirable aspects of existing phase-field models. The development of this phase-field model in a manner consistent with irreversible thermodynamics was described in detail in Wang et al. [19]. The nature of an anisotropic form of this phase-field model was characterized by McFadden et al. [20]; an asymptotic analysis was used to obtain the classical sharp interface free boundary problem that is recovered at leading order in the limit when the interface thickness is taken to zero in the phase-field model. This model is well suited for numerical computation and two recent computational studies have investigated the important aspects associated with solving the anisotropic phase-field equations and how the results obtained compare with sharp interface theories for dendritic growth from an undercooled melt [21,22]. Also, a comprehensive comparison between this phase-field model for a pure material and the corresponding sharp interface model has been performed for the morphological stability of a planar interface by Braun et al. [23].

Other relevant work concerns the development of phase-field models for the solidification of an alloy. Wheeler et al. [24,25] developed and analyzed two related phase-field models for an isothermal system, and Caginalp and Xie [26] introduced a phase-field model for a nonisothermal alloy. By combining aspects of the model for a pure material of Wang et al. [19] and those from the model for an isothermal alloy of Wheeler et al. [24], Warren and Boettinger [27] also produced a phase-field model for the treatment of a nonisothermal binary alloy. They used this model to compute two-dimensional, isothermal solute dendrites grown into a highly supersaturated solution. They included anisotropy in a similar manner to the previous phase-field calculations for a pure material and allowed for different solute diffusivities in the solid and liquid phases. They were able to produce qualitatively realistic solute patterns from an evolving sidebranched

solute dendrite. Better numerical techniques and more powerful computers are still required in order to treat the complete nonisothermal alloy dendrite.

In this paper, additional two-dimensional computations are performed using the model developed recently for a pure material [19]. The time-dependent heat and phase-field equations are solved numerically using finite-difference techniques on a uniform computational mesh for conditions simulating dendritic growth into an undercooled liquid at relatively high dimensionless undercoolings. The objective of these computations is to demonstrate that the phase-field model equations can be used to simulate observed behavior in dendritic growth experiments, such as the competition between two dendrite branches that result from the splitting of a growing solid particle, and the effect of time-periodic forcing applied to an isolated dendrite tip on the mechanism of sidebranch formation. The comparison between the computations and experiments is qualitative, since the conditions of the experiments cannot be modeled closely at the present time. Nevertheless, the phase-field computations exhibit many features of the physical experiments and can be used to provide considerable insight into the nature of the physical mechanisms associated with the complicated behavior of dendritic solidification. In the following section, the phase-field model equations are given and the model parameters are described in terms of the physical quantities familiar from the classical theory.

## 2. Governing equations

Phase-field models of solidification are typically derived from a Landau–Ginzburg or Cahn–Hilliard type of free-energy functional. The free-energy functional is comprised of a local free energy density and a gradient energy contribution related to spatial gradients of a phase-field variable or order parameter,  $\phi(x,t)$ , which is introduced as a consequence of this approach. For a pure material the free-energy density of the system is assumed to be a monotonic function of the

temperature,  $T(x,t)$ , and has the form of a double-well with respect to  $\phi$ . The two minima with respect to  $\phi$  represent the free energy of the solid and liquid phases for each temperature. In many of the previous developments of phase-field models, the free energy is used to obtain a kinetic equation for the phase field by requiring that it evolves in a manner such that the total free energy decreases monotonically in time; a modified form of the heat equation is assumed which includes an appropriate source term to account for the liberation of latent heat. Although this approach for deriving the phase-field model equations yields a viable set of equations for computations, the basis for the model as applied to nonisothermal systems is unsatisfactory from the point of view of thermodynamics.

For the computations here, we employ a recently developed phase-field model for which the governing equations are obtained via a more rigorous derivation by Wang et al. [19]. The development of the model was couched in the methodology of irreversible thermodynamics and employs an entropy functional to derive the governing equations in a manner similar to Penrose and Fife [28]. The nonisothermal phase-field model equations are obtained by requiring that they ensure positive local entropy production. A similar approach was also employed by Umantsev and Roitburd [29]. The ramifications of this type of derivation are addressed in Wang et al. and the relationship of the present model to existing phase-field models is discussed as well. Additionally, the present model possesses the computationally attractive feature that the values  $\phi \equiv 0$  and  $\phi \equiv 1$  correspond to the bulk solid and liquid phases, respectively, independent of the temperature. This feature was first employed by Kobayashi in his phase-field computations [17] and was also examined by Caginalp and Chen [30].

The phase-field model equations used for the computations here will be written in nondimensional form. Length has been scaled on some reference length scale  $w$  of say the dimensions of the domain, time on the corresponding thermal diffusion time  $w^2/\kappa$  (where  $\kappa$  is the thermal diffusivity), and temperature by setting  $T = T_M + \Delta T u$ , where  $T_M$  is the equilibrium melting tem-

perature and  $\Delta T$  is the undercooling (difference between the melting temperature and the initial temperature at the boundary of the domain). The following dimensionless governing equations for the temperature and phase field are obtained:

$$\frac{\partial u}{\partial t} + \frac{30g(\phi)}{S} \frac{\partial \phi}{\partial t} = \nabla^2 u, \quad (1)$$

$$\begin{aligned} \frac{\tilde{\epsilon}^2}{m} \frac{\partial \phi}{\partial t} = & \phi(1-\phi)\left(\phi - \frac{1}{2}\right) \\ & + 30g(\phi)\tilde{\epsilon}\alpha Su + \tilde{\epsilon}^2 \nabla^2 \phi, \end{aligned} \quad (2)$$

where  $g(\phi) = \phi^2(1-\phi)^2$ . This isotropic phase-field model is characterized by four dimensionless parameters:

$$S = \frac{c\Delta T}{L}, \quad (3)$$

$$\alpha = \frac{\sqrt{2} w L^2}{12c\sigma T_M} = \frac{\sqrt{2} w}{12 d_0}, \quad (4)$$

$$m = \frac{\mu\sigma T_M}{\kappa L} = \frac{\mu d_0 T_M}{\kappa}, \quad (5)$$

and

$$\tilde{\epsilon} = \frac{\delta}{w}, \quad (6)$$

where  $c$  is the specific heat per unit volume,  $L$  is the latent heat per unit volume,  $\sigma$  is the surface energy,  $\mu$  is the interface kinetic coefficient, and  $\delta$  is a measure of the interface thickness. The parameter  $S$  is the Stefan number or dimensionless undercooling (the quantity  $L/c$  is the unit of undercooling). The above definitions for the phase-field parameters  $\alpha$  and  $m$  show how they are related to the classical physical parameters which characterize the interface dynamics (i.e., interfacial energy and kinetic coefficient). We have introduced one common representation of the capillary length,  $d_0 = c\sigma T_M/L^2$ , into the parameter definitions to help elucidate their meaning and to simplify the characterization of  $\alpha$  and  $m$  for different materials. For a given material, the value of  $\alpha$  is determined by the choice of the length scale  $w$ . For unconstrained dendritic growth, there is no well-defined choice to use for this length scale. We find that choosing a length representative of the dendrite features (tip ra-

dius, sidearm spacing) for the given thermal undercooling conditions is most appropriate. The material parameters and the choice of the length scale for the calculations here will be specified in the next section.

Once the characteristic length scale  $w$  has been chosen, knowledge of the physical properties leaves one degree of freedom, namely  $\tilde{\epsilon}$ , which then is used to set the interface thickness and is the only additional model parameter associated with the phase-field approach. It is expected that in order to model the physical behavior correctly, the interface thickness must be sufficiently small compared to the interfacial macrostructures that are to be modeled; however, from a computational viewpoint, it is desirable for the interface thickness to be as large as possible in order that accurate solutions of the phase-field equations can be obtained for practical computational effort. It is useful to note that the quantity  $\tilde{\epsilon}\alpha$  that appears in Eq. (2) is equal to  $(\sqrt{2}/12)\delta/d_0$ , and thus gauges how the interface thickness compares to the capillary length.

It is well known that in order to obtain a well-defined operating state in models of dendritic growth, anisotropy in either the surface energy or interfacial attachment kinetics (or both) is necessary. Here, anisotropy is introduced by letting the coefficient of the gradient term in the entropy functional used to derive Eq. (2) depend on orientation (see Ref. [20]); the form of the anisotropy in the gradient term is characterized by

$$\tilde{\epsilon}(\theta) = \bar{\epsilon}\eta(\theta) = \bar{\epsilon}(1 + \gamma \cos k\theta).$$

The angle  $\theta$  is defined as the angle between  $\nabla\phi$  and the  $x$ -axis,  $\bar{\epsilon}$  is the mean value of the dimensionless interface thickness  $\tilde{\epsilon}$ ,  $\gamma$  is the magnitude of the anisotropy, and  $k$  specifies the mode number. As an example, in order to simulate a crystal with cubic structure a value of the mode number  $k = 4$  would be used. Values for the parameter  $\gamma$  have only been determined for a small number of materials. As a result, the characterization of the anisotropy for a real material is only approximate.

Rederiving Eq. (2) after including the variation of the gradient energy coefficient with orientation

yields a modified version of the phase-field equation:

$$\begin{aligned} \frac{\tilde{\epsilon}^2}{m} \frac{\partial \phi}{\partial t} = & \phi(1-\phi) \left\{ \phi - \frac{1}{2} [1 + A_n N(x, y, t)] \right\} \\ & + 30\tilde{\epsilon}\alpha S \phi^2 (1-\phi)^2 u \\ & + \tilde{\epsilon}^2 \left[ -\frac{\partial}{\partial x} \left( \eta(\theta) \eta'(\theta) \frac{\partial \phi}{\partial y} \right) \right. \\ & \left. + \frac{\partial}{\partial y} \left( \eta(\theta) \eta'(\theta) \frac{\partial \phi}{\partial x} \right) + \nabla \cdot (\eta^2(\theta) \nabla \phi) \right]. \end{aligned} \quad (7)$$

In addition, the first term on the right-hand side of the equation has been modified to include the function  $N(x, y, t)$  which allows for the addition of noise within the interfacial region. The magnitude of the noise function  $N$  varies between  $\pm 1$ , and the level of the imposed noise is characterized by the parameter  $A_n$ , which will generally be small. Including noise in this manner has been done in previous phase-field computations [17,21]. The actual form of the noise function employed depends on the nature of the physical behavior that is to be investigated. In order to simulate the irregular sidebranched structure typically observed in dendritic growth, a random function in space (within the interfacial region) and time is used for the function. For simulating regular forcing of the dendrite tip, a sinusoidal function of time is used for  $N$  and is applied only at the location of the moving dendrite tip. Both types of noise are employed for the calculations presented here and a more complete description of the noise implementation is given when the specific simulations are discussed.

In the phase-field model, the interface is represented by a range of contour levels of  $\phi$ , e.g.,  $0.1 \leq \phi \leq 0.9$ . In order to compute the anisotropic behavior, the orientation angle is determined in terms of the phase field  $\phi$  using the following relation for the normal vector:

$$\hat{n} = \frac{\nabla \phi}{|\nabla \phi|} = \cos \theta \hat{x} + \sin \theta \hat{y}.$$

From this expression we have the definition

$$\tan \theta = \frac{\phi_y}{\phi_x},$$

and, in addition, we obtain

$$\theta_x = \frac{\phi_x \phi_{xy} - \phi_y \phi_{xx}}{|\nabla \phi|^2}, \quad \theta_y = \frac{\phi_x \phi_{yy} - \phi_y \phi_{xy}}{|\nabla \phi|^2}.$$

These relations are used to compute the terms in Eq. (7) which arise from evaluating the derivatives of  $\eta(\theta)$ .

By conducting an asymptotic analysis of the phase-field equations in the limit  $\tilde{\epsilon} \rightarrow 0$  with  $S$ ,  $\alpha$ , and  $m$  of order one, the classical description of an appropriate free boundary problem is recovered. A thorough development of the interfacial conditions for the present anisotropic phase-field model with the assumed form for  $\tilde{\epsilon}(\theta)$  is given in Ref. [20]; the details of this type of analysis were first given by Caginalp [31] for the isotropic form of a different phase-field model. The free boundary problem satisfied by the leading-order temperature field for the phase-field model given by Eq. (1) and Eq. (7) is

$$\frac{\partial u}{\partial t} = \nabla^2 u, \quad (8)$$

with interfacial boundary conditions

$$\left( \frac{\partial u}{\partial n} \right)_{\text{Solid}}^{\text{Liquid}} = -\frac{v_n}{S}, \quad (9)$$

and

$$u = -\Gamma \left( \frac{v_n}{m\eta(\theta)} + [\eta(\theta) + \eta''(\theta)] \mathcal{K} \right), \quad (10)$$

where  $\Gamma = d_0 T_M / w \Delta T$  is a dimensionless form of the capillary length,  $v_n$  is the dimensionless normal velocity of the interface into the liquid and  $\mathcal{K}$  is the dimensionless interfacial curvature (measured positive for convex projections into the liquid). The interfacial boundary condition Eq. (10) reduces to the anisotropic form of the Gibbs–Thomson equation when  $v_n = 0$ ; the term including  $v_n$  incorporates the effect of interface kinetics. It is important to emphasize here that introducing anisotropy by allowing  $\tilde{\epsilon}$  to depend on  $\theta$  modifies both the term proportional to velocity and the term proportional to curvature, i.e., anisotropic interface kinetics and surface energy are obtained.

### 3. Numerical computations

The objective here is to use the anisotropic phase-field model to simulate the growth of a two-dimensional dendrite into an undercooled liquid subject to either a specific initial configuration or to time-dependent forcing of the dendrite tip. Two previous numerical studies using the same anisotropic phase-field model for a pure material have evaluated the behavior of the model and the numerical issues related to solving the phase-field equations accurately [21,22]. Two-dimensional dendritic structures with four- and six-fold symmetry have been calculated. The same numerical techniques are used for the computations here, so only a brief summary of the techniques and computational issues is given in what follows.

The governing equations given by Eq. (1) and Eq. (7) are discretized spatially using second-order finite differences on a uniform grid characterized by mesh spacings  $\Delta X$  and  $\Delta Y$  in the  $x$  and  $y$  coordinate directions, respectively; for the temporal discretization we introduce the time step  $\Delta t$ . In order to maximize the computational efficiency, we employ explicit time-differencing on the  $\phi$  equation which is nonlinear and is highly complicated in the anisotropic formulation. The heat equation is linear in the temperature  $u$  but contains the source term depending on  $\phi$ . For the present calculations, the thermal field diffuses more rapidly, so to avoid the diffusive stability requirement, the alternating-direction implicit method (ADI) is used on Eq. (1).

For the two-dimensional rectangular computational domain, vanishing Neumann conditions for both  $\phi$  and  $u$  are applied at the boundaries, which have the scaled dimensions of  $X_L$  and  $Y_L$  in the  $x$  and  $y$  coordinate directions, respectively. From the chosen definition of the dimensionless variables, the value  $u = 0$  corresponds to the melting temperature of the pure material, whereas  $u = -1$  is the initial undercooling temperature (the dimensional undercooling is  $\Delta T$ ). Because the computational domain is thermally insulated, the value of the dimensionless undercooling  $S$  determines the portion of the domain which can be solidified. Thus, with fixed grid

numerical techniques, the computations are facilitated by larger values of  $S$ . The computations are started by introducing a small region of solid ( $\phi = 0$ ,  $u = 0$ ) at one end of the domain with the remainder of the domain being undercooled liquid ( $u = -1$ ). The shape of the initial solid region is circular with an initial radius denoted by  $r_0$ .

The experiments we are attempting to model are typically conducted using transparent systems such as succinonitrile or pivalic acid because they provide good physical analogs to metallic systems and allow direct visual observation of the solidification morphology. However, these materials cannot be undercooled substantially, with typical dimensionless experimental undercoolings achieved in the range  $S = 0.002$ – $0.1$  [32]. As discussed above, the present phase-field computations require relatively large dimensionless undercoolings around  $S = 0.5$ , since for high undercooling the solid encompasses a larger portion of the computational domain and the thermal boundary layer in the liquid is sufficiently small so the effect of the adiabatic outer boundaries is less pronounced. We choose  $S = 0.5$  as the dimensionless undercooling for all the calculations presented here.

Since large undercoolings are attainable in the solidification of metals such as nickel [33], we choose the property values for pure nickel to determine the model parameters. The values of the capillary length,  $d_0$ , for nickel and succinonitrile are similar. The principal difference in the model parameters is the value of the mobility,  $m$ , which is larger for succinonitrile due to its lower thermal diffusivity. The larger  $m$  value would require more computation time because of the explicit time-differencing. For these reasons nickel is the more convenient material choice for the computations. The required material parameters for nickel are readily available (see, for example, Ref. [34]). Here we have used the values:  $\sigma = 3.7 \times 10^{-5}$  J/cm<sup>2</sup>,  $T_m = 1728$  K,  $L = 2350$  J/cm<sup>3</sup>,  $c = 5.42$  J/K cm<sup>3</sup>, and  $\kappa = 0.155$  cm<sup>2</sup>/s. The kinetic coefficient,  $\mu$ , is not as well established as the other material parameters. An estimate for the kinetic coefficient for nickel is given by Coriell and Turnbull [34]; they obtained  $\mu =$

200 cm/K s which yields the dimensionless parameter  $m = 0.035$ . In order to determine the dimensionless parameters  $\alpha$ , one must choose a value for the reference length,  $w$ . Based on preliminary estimates of the tip radius at the chosen undercooling level, we arrived at a length scale value  $w = 2.1 \times 10^{-4}$  cm which yields the parameter value  $\alpha = 400$  in the definition Eq. (4).

It remains to specify the interface thickness, the grid resolution, the size of the domain, the anisotropy parameters, and the noise function in Eq. (7). Here, we discuss the interface thickness and grid resolution. The remaining quantities are specified when discussing the results for the specific computation.

The parameter  $\bar{\epsilon}$  determines the average thickness of the interface, but owing to certain scaling choices in the model formulation, it is not an accurate measure of actual interface thickness obtained in the numerical computations. If the interface is defined by the values of  $\phi$  between 0.1 and 0.9, then the actual interface width is more than  $6\bar{\epsilon}$ , whereas for values of  $\phi$  between 0.01 and 0.99, the actual interface width is about  $13\bar{\epsilon}$ . These measures of the actual interface thickness are important when trying to evaluate the required grid resolution for accurate solutions of the phase-field equations. As demonstrated in Wheeler et al. [21], a good estimate for the required grid spacing is that  $\Delta X \approx \bar{\epsilon}$ . Similar findings have been reported by Caginalp and Socolovsky [15,35] for a different phase-field model. Depending on how one chooses to define the width of the interface, this choice will yield somewhere between 6–13 grid points across the interfacial layer. It was found that the condition  $\Delta X \leq \bar{\epsilon}$  is required in order to obtain good quantitative behavior, such as a less than 5% relative change in a calculated quantity like the dendrite tip velocity. However, it is possible to obtain the same overall qualitative behavior in the computations by using the criterion  $\Delta X \leq 2\bar{\epsilon}$ . This less stringent requirement had to be used for the computations that required a large computational domain.

Values for the parameter  $\bar{\epsilon}$  from  $6.25 \times 10^{-3}$  to  $2.5 \times 10^{-3}$  have been used in various computations with the present phase-field model. As re-

ported in Wheeler et al. [21], smaller values of  $\bar{\epsilon}$  yield a better representation of quantitative measures like the Gibbs–Thomson condition from the corresponding sharp interface free-boundary problem. But small values of  $\bar{\epsilon}$  are not practical for large-scale dendrite simulations. Thus, for all the computations presented here,  $\bar{\epsilon} = 6.25 \times 10^{-3}$ . We have tested to a limited extent the effect of the interface thickness for the range of  $\bar{\epsilon}$  listed above on the computed behavior of the phenomena simulated here. The qualitative behavior is found not to depend on the interface width over this range of variation. However, accurate quantitative characterization of the complicated physical phenomena considered here will not be possible until further developments are achieved in numerical techniques and computer hardware.

## 4. Results and discussion

In this section results are reported from computations that attempt to simulate observed phenomena in recent experiments on dendritic growth. All the computations presented have four-fold anisotropy, so the mode number  $k = 4$  is used in the function  $\eta(\theta)$  which appears in Eq. (7). This corresponds to preferred growth in the  $x$  and  $y$  coordinate directions. The magnitude of the anisotropy level,  $\gamma$ , ranges between 0.01–0.02. Before presenting the results for the specific simulations, we summarize the phase-field model parameters that are held fixed in all the computations reported here:  $S = 0.5$ ,  $\alpha = 400$ ,  $m = 0.035$ , and  $\bar{\epsilon} = 6.25 \times 10^{-3}$ .

### 4.1. Cleaving

A recent series of experiments on the USMP-2 mission of the space shuttle were reported by Glicksman et al. [36]. In these experiments, succinonitrile dendrites were grown under microgravity conditions in order to suppress the effects of buoyant convection. An isolated dendrite is grown from the end of a capillary tube placed within the undercooled succinonitrile. In some instances in the microgravity experiments, it has been ob-

served that as the dendrite tip with a given radius leaves the tube it can split and form two dendrites with a smaller radius [37]. In particular, the initial dendrite tip grows more slowly and with a larger radius than expected by conventional dendrite tip growth theory. After a short period of steady growth the tip splits and two dendrites emerge that grow in parallel. The two dendrites compete with one another as they grow until one of them predominates over the other by growing faster and eventually causing the slower dendrite to be displaced from the original growth direction. The dendrite that finally emerges grows with a tip radius and velocity consistent with dendrite growth theory. This phenomenon results in a dendrite which has a deep gash in the body of its main branch structure as if it has been cleaved. We choose to refer to this type of event as a “cleaving” phenomenon. In Fig. 1 we show a sequence of photographs of a dendrite exhibiting this cleaving behavior taken during the recent space-flight experiments conducted by Glicksman et al. [36].

We have performed computations using the phase-field model described here which simulate some of this cleaving behavior, at least, qualitatively: the tip splitting, the dendrite branch competition, and the eventual predominance of a single dendrite. As already discussed, the phase-field computations require high undercoolings. The experiments are conducted at low undercoolings, so we are unable to reproduce the exact conditions of the experiment. Again, the main difficulty at low undercoolings is that the Peclet number is small, and the temperature has a much larger length scale than that of the dendrite tip radius. This length scale separation requires com-

putations on very large domains which would require more computational resources than can reasonably be provided at the present time.

The cleaving simulation was performed on a computational mesh that had  $\Delta X = \Delta Y = 0.01$  ( $\Delta X = 1.6 \bar{\epsilon}$ ) and a time step  $\Delta t = 1.25 \times 10^{-4}$ . Because at high undercooling the extent of the temperature field is localized, we used a series of increasingly larger domains with the same height  $Y_L = 12$ , but with lengths of  $X_L = 6, 9$  and 15. For the largest extent of the domain ( $1500 \times 1200$  grid points), the computations required a little less than 2 CPU hours on a Cray-YMP to calculate for 8000 time steps or a single dimensionless time unit. For this simulation (as well as previous simulations of dendritic growth [17,21,22]) a random function is used for  $N(x, y, t)$  in Eq. (7) in order to produce irregularity in the sidearm formation. For this calculation, a noise amplitude  $A_n = 0.025$  was prescribed, and as already discussed is applied within the interfacial region throughout the computation.

For the cleaving simulation, the seed crystal consists of a semicircle of radius  $r_0 = 0.1$  which is located half way up on the extreme left of the domain. Fig. 2 shows the development of the seed from the initial time and at four early times in the computation. Plotted in the figure are three contour levels of the phase variable ( $\phi = 0.1, 0.5, 0.9$ ). Only the region in the vicinity of the seed is shown, and at this high magnification the three contour levels can be clearly distinguished. The initial condition is imposed as if the interface was a sharp boundary, so only a single line appears at  $t = 0$ . Because of the four-fold anisotropy, the solid grows the fastest in the  $x$  and  $y$  coordinate directions. For the calculation, an anisotropy

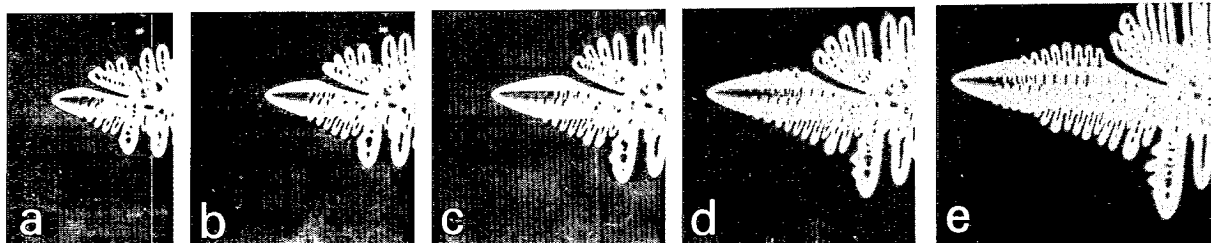


Fig. 1. sequence of photographs of a succinonitrile dendrite showing the cleaving phenomenon, taken by Glicksman et al. [36] during the recent USMP-2 dendrite growth experiment. The undercooling of the liquid is 0.211 K.



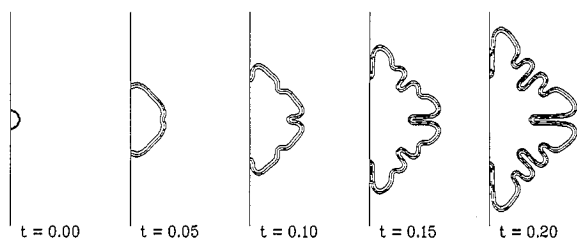


Fig. 2. Evolution of the initial semi-circular solid region ( $t = 0$ ) at early computation times. The phase-field contours ( $\phi = 0.1, 0.5, 0.9$ ) are plotted at the four nonzero time levels listed. Only a very small portion of the computational domain is shown at each time level at these early times.

magnitude of  $\gamma = 0.015$  was used. Already, by  $t = 0.05$ , there is evidence that the evolving interface has split along the directions of fastest growth. At time  $t = 0.1$ , there is also splitting along the  $45^\circ$  axes. By  $t = 0.2$ , two evolving dendrites growing in the  $x$  (horizontal) direction are clearly evident. The growth and competition between these two dendrite branches will be followed as time proceeds in the calculation.

In Figs. 3a–3d, we show the computed solutions at four later times ( $t = 1, 2.1, 3.6, 4.4$ ). At each of the time levels, contours of the phase

variable (same  $\phi$  values as Fig. 1) are shown in the lower half, while the upper half of each time level shows the corresponding isotherms (11 values). In Fig. 3a, the two dendrite tips, which at this relatively early time have grown to the same extent, show side branching activity but it is confined to the exterior sides of each dendrite. This occurs because the cleft between the dendrites is nearly isothermal and little thermodynamic driving force remains to promote sidebranches. At  $t = 2.1$ , Fig. 3b, the lower dendrite has advanced ahead of its neighbor and is surrounded by correspondingly cooler liquid, which further promotes its growth. Growth proceeds with the inferior dendrite growing slightly off axis, and being progressively displaced. By  $t = 3.6$ , Fig. 3c, the superior lower dendrite has advanced sufficiently that its exposed upper boundary experiences enough of a temperature gradient to promote sidebranch formation there as well. This releases latent heat in front of the inferior dendrite which acts to reduce the thermodynamic driving force for the slower dendrite still further, i.e., the sidebranch formation acts to thermally screen the inferior dendrite. By  $t = 4.4$ , Fig. 3d, the inferior dendrite tip has been stopped from growing by the pres-

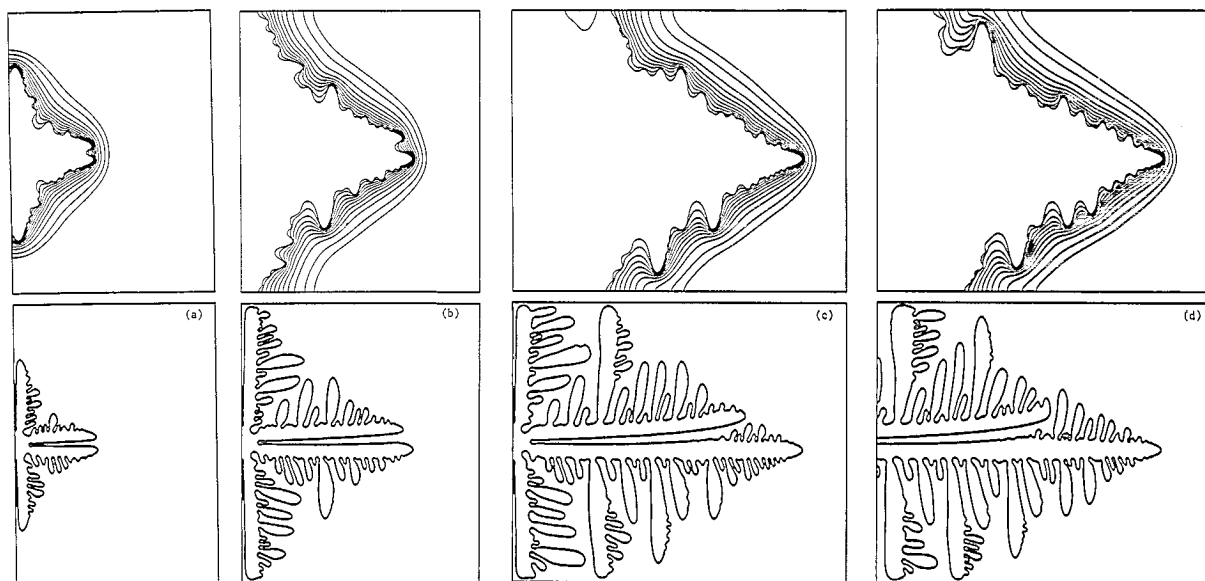


Fig. 3. Simulation of cleaving phenomenon for dendrite with four-fold anisotropy ( $k = 4$ ) and anisotropy level  $\gamma = 0.015$ . The computed isotherms (top) and phase-field contours (bottom) are shown at four time levels: (a) 1.0, (b) 2.1, (c) 3.6 and (d) 4.4.

ence of a large sidearm from the superior dendrite just ahead of it. Growth in the inferior dendrite only takes place subsequently in secondary and tertiary arms. We note that as the superior dendrite moves ahead of the other branch its tip radius increases somewhat as it becomes the dominate main dendrite stem; this feature was qualitatively observed in the recent space-flight experiments.

We investigated the initial growth of the seed in some detail and found that the tip splitting event to be unaffected by reducing the interface thickness. It was found, however, that the initial growth of the seed was sensitive to the initial conditions and their representation on the finite difference grid. One would expect that the tip splitting occurs when the initial radius of the seed crystal is larger than the critical radius for morphological instability with the given surface energy and interfacial kinetics. We attempted to identify a critical radius by varying the initial radius in the computations. However, this proved to be impractical owing to the difficulty of representing the initial circular seed consistently on a fixed rectangular grid as the radius was reduced, which resulted in the critical radius depending on the grid resolution. Variability introduced by numerical approximation remains a subtle problem when modeling highly unstable physical systems. Thus, for the computations the initial radius was chosen sufficiently large to yield tip splitting irrespective of the interface thickness and grid resolution used. For the actual system, the cleaving phenomena is sensitive to the experimental conditions. Indeed, in the space-flight experiments the phenomenon was only observed at the lowest undercoolings (less than 0.4 K). This is the regime where thermal convection is active, even in the microgravity environment of the space-flight experiment [36], and so convection may play a role in stimulating the tip splitting. Moreover, the cleaving phenomenon is also observed in terrestrial experiments, where convection is important over a larger range of undercooling, but the dendrite competition phase is not. This may occur because terrestrial convection can promote one dendrite to such an extent that the competition period is too short to observe.

#### 4.2. Tip pulsing

The mechanism of sidebranch formation in dendritic growth continues to be the subject of considerable research. In the last few years, a number of experiments have attempted to gain understanding of sidearm formation by studying the effect of imposed periodic forcing of the dendrite tip on the creation of sidebranches. Two separate groups conducted forcing experiments at about the same time. One group, Cummins and co-workers, have reported results from two distinct sets of experiments [38,39]. The first set of experiments were conducted using succinonitrile containing acetone, whereas the second set of experiments used pivalic acid. In both cases, a single dendrite was grown in a glass capillary (essentially two-dimensional) and the periodic forcing was achieved via a brief localized heat pulse from a laser applied near the dendrite tip. In the experiments of Bouissou et al. [40], the periodic forcing of the tip was obtained by the imposition of an oscillating flow in the liquid; the material was a mixture of pivalic acid and ethanol, and in contrast to the first group, the dendrites were fully three-dimensional. Similar behavior was observed in the experiments of the two individual groups. As a result of the periodic forcing, the production of sidebranches becomes regular when the frequency of the forcing is in the range where a resonant response is obtained. Fig. 4 shows two of the experimentally observed dendrites published in Williams et al. [39]. Fig. 4a shows the irregular sidebranch structure obtained in the absence of applied forcing; Fig. 4b shows the dendrite obtained under applied periodic forcing at a frequency they determined to be close to the natural frequency for the system.

Here, we employ the anisotropic phase-field model in an attempt to simulate the dendrite tip pulsing experiments in a qualitative manner. To simulate the behavior of periodically forcing the tip of a growing dendrite the following form for the noise function  $N$ , which appears in Eq. (7), is employed:

$$N(x, 0, t) = \begin{cases} 0 & t < t_p \\ \sin(2\pi ft) & t > t_p, \end{cases}$$

where  $f$  is the frequency of the imposed forcing; as mentioned in Section 2, the amplitude of the forcing level is represented by  $A_n$ . The value  $t_p = 0.1$  was used to allow the needle shaped dendrite to form before the periodic forcing was applied. The forcing amplitude was  $A_n = 0.005$  in all cases.

The initial solid seed for the pulsing calculations was placed in the lower left corner of the rectangular computational domain ( $X_L = 7.5$ ,  $Y_L = 3.75$ ). Thus, the primary dendrite tip grows along the bottom of the computational domain in the  $x$  direction. This was done for two reasons: by employing symmetry we can perform the com-

putation using only one-half of the domain, and since the tip grows along the domain boundary it simplifies implementing the forcing and analyzing the tip evolution. In displaying the computed solutions for  $\phi$  and  $u$ , we reflect them about the  $x$  axis to achieve the representation of a complete needle dendrite.

The tip pulsing simulations were performed on a computational mesh that had  $\Delta X = \Delta Y = 0.0125$  ( $\Delta X = 2 \bar{\epsilon}$ ) and a time step  $\Delta t = 2.0 \times 10^{-4}$ . The anisotropy had the magnitude  $\gamma = 0.02$  for these calculations. We first conducted a “control” computation in the absence of any forcing. The resulting dendrite, displayed in Fig. 5a, shows only one sidebranch at the root of the dendrite as a result of the initial evolution; otherwise, there is no sidearm production from the growing tip, and a simple needle dendrite shape is obtained. Calculations were performed for dimensionless pulsing frequencies in the range 2.5 to 25. Figs. 5b and 5c show the periodic sidearm production for the imposed forcing frequencies 15 and 20, respectively. All three computed dendrites in Fig. 5 are shown at the same dimensionless time,  $t = 1.5$ . A uniformly spaced sidearm structure is clearly visible in the two forced computations with the earlier sidebranches affected by coarsening. However, the sidearm production is much less pronounced with smaller sidearms more closely spaced together at the higher frequency  $f = 20$ , suggesting that the frequency  $f = 15$  may be closer to the resonant or natural frequency for the system. Although not shown, the dendrite calculated for the highest frequency of  $f = 25$  again shows no sidearm production.

We assess the effect of the pulsing by determining the perimeter of the dendrite by integrating the quantity  $\phi(1 - \phi)$ , which is nonzero only in the interfacial region, over the area of the computational domain. Dividing this integrated quantity by the average interface thickness yields an estimate for the perimeter of the dendrite. This measure of the perimeter enables a quantitative comparison of the effectiveness of the periodic forcing in terms of sidearm production. In Fig. 6 we display the perimeter,  $P$ , of the dendrite calculated at the dimensionless time,  $t = 1.5$ , for each of the applied pulsing frequencies. There

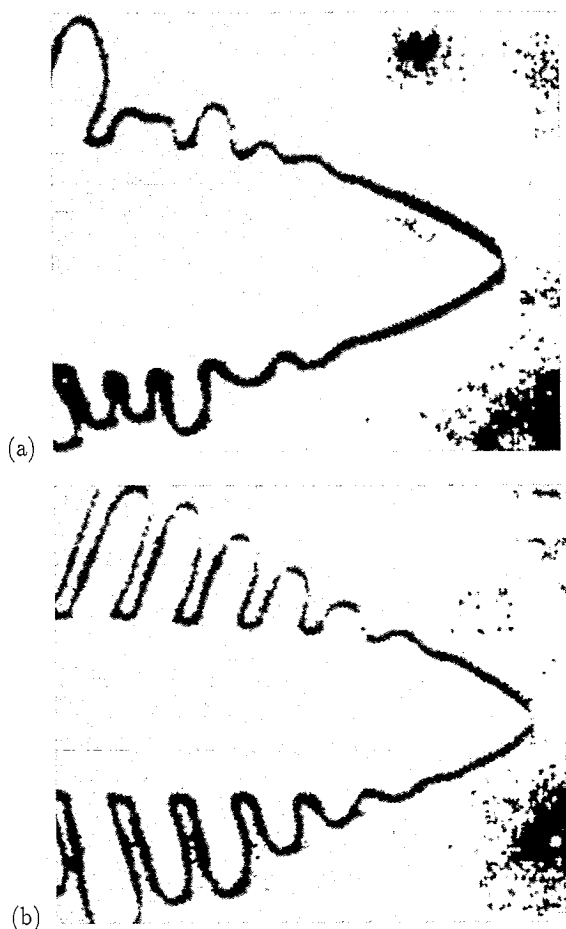


Fig. 4. Experimentally observed dendritic structure in pivalic acid published by Williams et al. [39]. Irregular sidearm formation occurs in the absence of forcing (a); regular sidearm production results from periodic forcing of the tip by a heat pulse from a laser (b).

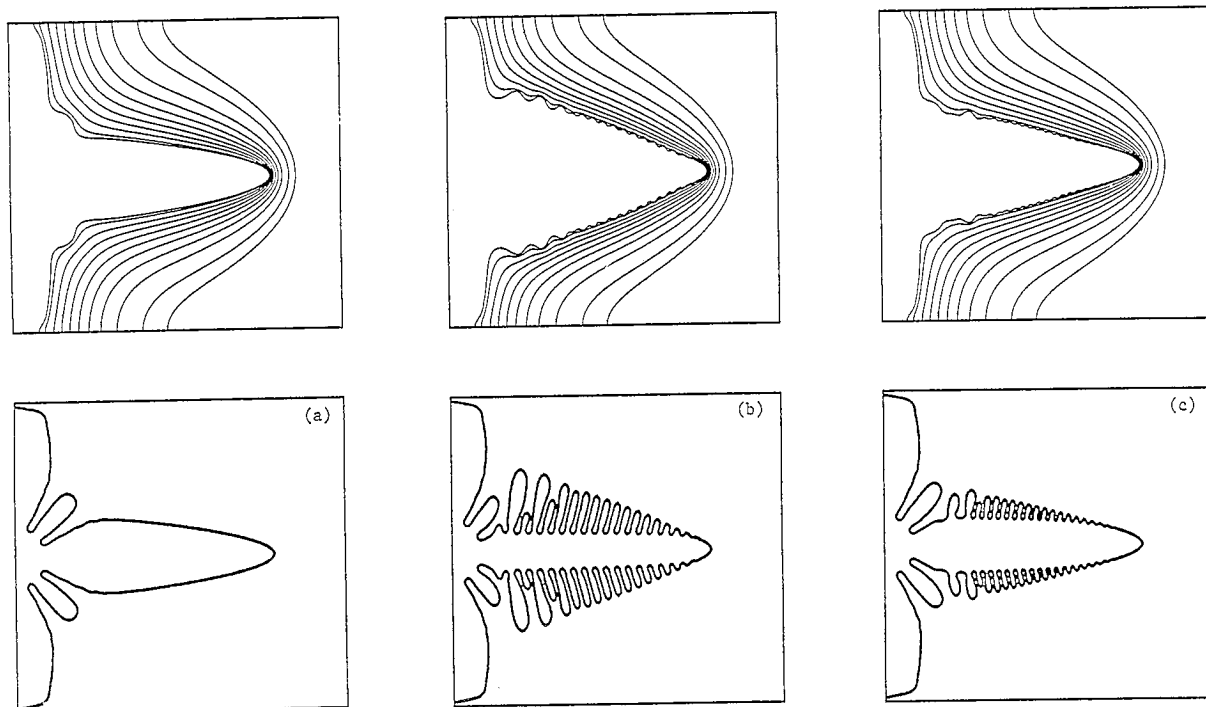


Fig. 5. Response of dendritic growth to periodic tip pulsing. The computed isotherms (top) and phase-field contours (bottom) at time level  $t = 1.5$  are shown for three values of the forcing frequency: (a)  $f = 0$  (no forcing), (b)  $f = 15$ , (c)  $f = 20$ . Note that the computations are performed for only one-half of the domain shown; the solutions have been reflected about the horizontal centerline.

is clearly a resonant response of the dendrite to the applied forcing with the maximum degree of sidearm area produced for a dimensionless resonant frequency of about 14. This response is evident in the dendrite structure obtained for the two frequencies shown in Fig. 5. In the range of response frequencies, the frequency of the sidearm production per unit time was found to be the same as that of the imposed pulsing frequency (i.e., one sidearm is formed for each pulse). The effect of the imposed forcing is characterized in Fig. 7, where we display the tip radius, the tip temperature, and the tip velocity as a function of time for the computation with pulsing frequency  $f = 15$ . It is interesting that the response of the dendrite tip to the forcing is primarily evident through the time dependence of the tip radius. This is in contrast to the tip velocity and temperature of the dendrite which are only very weakly affected by the imposed pulsing, with a relative variation in amplitude about a factor of ten less than that of the tip

radius. We also note that the tip radius oscillates predominately with the same frequency of the applied pulsing, whereas the waveform for the tip velocity and tip temperature is more complicated, however, the mean values of these three quantities are essentially the same as those for the unforced case.

Barber, Barbieri and Langer [41] have provided a theoretical description of the sidearm response to periodic forcing at the dendrite tip. They analyzed the governing equations of the symmetric model of solidification linearized about the Ivantsov solution, using the WKB asymptotic method in the limit of small Peclet number. The model does not include any form of anisotropy. They showed that disturbing the tip by a perturbation of a single frequency gives rise to a selective amplification process whereby an interfacial wave (representing a sidebranch) is generated and travels down the dendrite stem. Initially the magnitude of the wave is amplified, but ultimately, sufficiently far down the dendrite stem, it

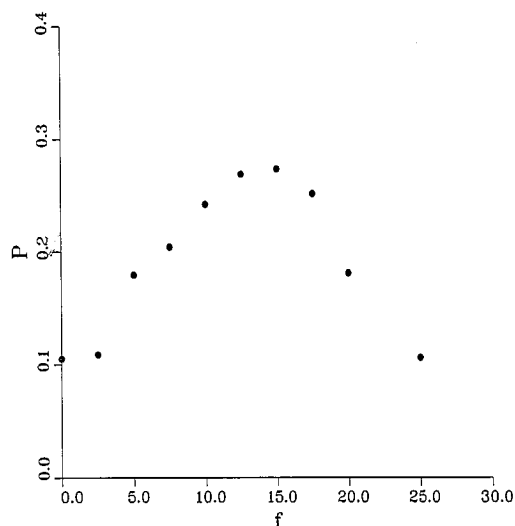


Fig. 6. Plot of the solid perimeter (as a measure of sidearm formation) versus the periodic forcing frequency. The perimeter is determined for individual phase-field computations at the same time level in each calculation ( $t = 1.5$ ).

is damped out. The position of maximum amplification experienced by the wave depends on its frequency; the position on the dendrite stem of maximum amplification increasing with decreasing frequency. As a consequence of this they predict that the resonant response of a sidearm depends on its position along the dendrite stem. The theory predicts resonant frequencies typical of the natural time scale of the tip,  $R/V$ , where  $R$  is the tip radius and  $V$  is its velocity. In terms of the nondimensionalization used here, we estimate the range of dimensionless resonant frequencies from about 35 for a sidearm 2 tip radii from the tip to a frequency of about 14 for a sidearm 32 tip radii back from the tip. The perimeter computed here and given in Fig. 6 to characterize the resonant response is obtained from the sidearm production averaged over a length of more than 100 tip radii. Nevertheless, the value of the resonant frequency obtained from the perimeter plot ( $f \approx 14$ ) is within the range of values predicted by the Barber, Barbieri and Langer theory.

To our knowledge, the computations presented here represent the first attempt at using the phase-field method to investigate numerically the response to imposed tip forcing. Owing to the

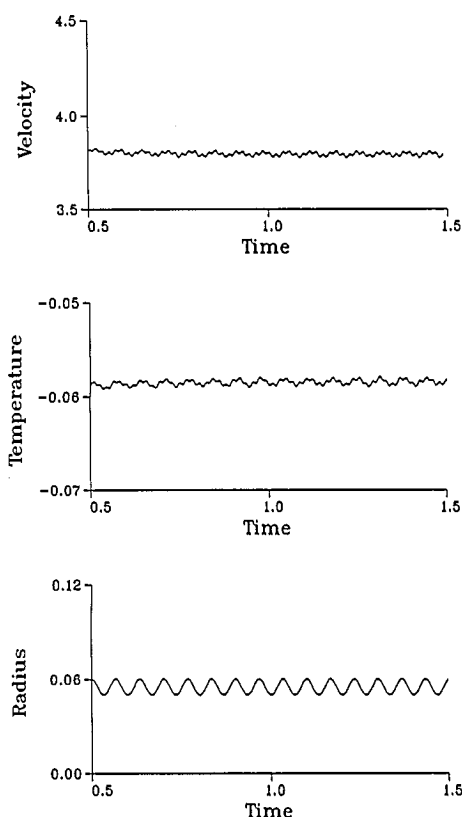


Fig. 7. Plot of the dimensionless tip velocity, tip temperature, and tip radius as a function of computation time for a forcing frequency  $f = 15$ . The dendritic structure for this computation is shown in Fig. 5b.

significant difference in conditions between the computations and the existing experiments, a more elaborate quantitative comparison is not attempted here, but remains the focus of current efforts being carried out in conjunction with better numerical solution techniques.

## 5. Conclusions

In this paper we have shown that the phase-field description of solidification can be used to simulate realistic phenomena qualitatively as observed in recent dendrite growth experiments. In particular, for growth into an undercooled melt, we have simulated a cleaving event, where an evolving solid seed splits forming two competing branches. One of the branches eventually pre-

dominates and becomes a primary sidebranched dendrite, while the growth of the other branch is suppressed. Also, we studied the effect of time-periodic forcing of an isolated dendrite tip on the mechanism of sidebranch formation. The qualitative behavior observed in tip forcing experiments is well represented by the phase-field computations. Additionally, we note that other realistic features of dendritic growth, such as sidearm coarsening, tertiary sidearm formation, and the inclusion of a liquid island in the solid are successfully simulated (see Fig. 3).

The phase-field approach is a promising method at present for simulating a variety of complicated solidification phenomena. Although currently it is not practical to verify convergence of the phase-field computations in large-scale simulations, the results presented show many of the qualitative features observed in recent experiments of dendritic growth. With current computer hardware and employing uniform-mesh schemes, the phase-field method remains limited to growth under highly undercooled conditions, which are not typically employed in the experiments. Future developments in hardware and software (e.g., adaptive techniques specifically designed for the phase-field approach) should enable computations in the parameter ranges of the dendritic growth experiments which, if successful, will yield a better quantitative comparison between the computations and the experiments. Also, we note that recent developments in adaptive finite elements, boundary integral methods, and sophisticated front tracking techniques are providing better capabilities for solving the free-boundary problem with complex dendritic morphology, and simulations based on these newer techniques will complement and provide more insight into the phase-field computations.

## Acknowledgements

The authors are grateful for discussions with R.J. Braun and S.R. Coriell, and wish to thank H.Z. Cummins for the permission to include the experimental figure. This work was performed with partial support from the Applied and Com-

putational Mathematics Program of DARPA, the Microgravity Science and Applications Program of NASA and EPSRC, UK.

## References

- [1] J.W. Cahn and J.E. Hilliard, *J. Chem. Phys.* 28 (1958) 258.
- [2] B.I. Halperin, P.C. Hohenberg and S.-K. Ma, *Phys. Rev. B* 10 (1974) 139.
- [3] S.M. Allen and J.W. Cahn, *Acta Met.* 27 (1979) 1085.
- [4] J.S. Langer, (1978), unpublished notes.
- [5] G.J. Fix, in: *Free Boundary Problems: Theory and Applications*, Eds. A. Fasano and M. Primicerio (Pitman, Boston, 1983) p. 580.
- [6] J.S. Langer, in: *Directions in Condensed Matter Physics*, Eds. G. Grinstein and G. Mazenko, (World Scientific, Philadelphia, 1986) p. 165.
- [7] J.B. Collins and H. Levine, *Phys. Rev. B* 31 (1985) 6119.
- [8] G. Caginalp, in: *Applications of Field Theory to Statistical Mechanics*, Ed. L. Garrido, *Lecture Notes in Physics* No. 216 (Springer, Berlin, 1985) p. 216.
- [9] G. Caginalp, *Arch. Rational Mech. Anal.* 92 (1986) 205.
- [10] G. Caginalp and P. Fife, *Phys. Rev. B* 33 (1986) 7792.
- [11] G. Caginalp, *Ann. of Phys.* 172 (1986) 136.
- [12] G. Caginalp and P. Fife, *Phys. Rev. B* 34 (1986) 4940.
- [13] G. Caginalp and J.-T. Lin, *IMA J. Appl. Math.* 39 (1987) 51.
- [14] J.-T. Lin, *SIAM J. Numer. Anal.* 25 (1988) 1015.
- [15] G. Caginalp and E.A. Socolovsky, *J. Comput. Phys.* (1991) 85.
- [16] A.R. Umantsev, V.V. Vinogradov and V.T. Borisov, *Soviet. Phys. Cryst.* 31 (1986) 596.
- [17] R. Kobayashi, *Physica D* 63 (1993) 410.
- [18] R. Kobayashi, *Exp. Math.* 3 (1994) 59.
- [19] S.-L. Wang, R.F. Sekerka, A.A. Wheeler, B.T. Murray, S.R. Coriell, R.J. Braun and G.B. McFadden, *Physica D* 69 (1993) 189.
- [20] G.B. McFadden, A.A. Wheeler, R.J. Braun, S.R. Coriell and R.F. Sekerka, *Phys. Rev. E* 48 (1993) 2016.
- [21] A.A. Wheeler, B.T. Murray and R.J. Schaefer, *Physica D* 66 (1993) 243.
- [22] B.T. Murray, W.J. Boettinger, G.B. McFadden and A.A. Wheeler, in: *Heat Transfer in Melting, Solidification, and Crystal Growth*, Eds. I.S. Habib and S. Thynell (ASME HTD-234, New York, 1993) p. 67.
- [23] R.J. Braun, G.B. McFadden and S.R. Coriell, *Phys. Rev. E* 49 (1994) 4336.
- [24] A.A. Wheeler, W.J. Boettinger and G.B. McFadden, *Phys. Rev. A* 45 (1992) 7424.
- [25] A.A. Wheeler, W.J. Boettinger and G.B. McFadden, *Phys. Rev. E* 47 (1993) 1893.
- [26] G. Caginalp and W. Xie, *Phys. Rev. E* 48 (1993) 1987.
- [27] J.A. Warren and W.J. Boettinger, *Acta Met.* 43 (1995) 689.

- [28] O. Penrose and P.C. Fife, *Physica D* 43 (1990) 44.
- [29] A.R. Umantsev and A.L. Roitburd, *Soviet Phys. Solid State* 30 (1988) 651.
- [30] G. Caginalp and X. Chen, in: *On the Evolution of Phase Boundaries*, Eds. M.E. Gurtin and G.B. McFadden, IMA Volumes in Mathematics and its Applications, Vol. 43 (Springer, Berlin, 1991) p. 1.
- [31] G. Caginalp, *Phys. Rev. A* 39 (1989) 5887.
- [32] S.-C. Huang and M.E. Glicksman, *Acta Met.* 29 (1981) 701.
- [33] R. Willnecker, D.M. Herlach and B. Feuerbacher, *Phys. Rev. Lett.* 62 (1989) 2707.
- [34] S.R. Coriell and D. Turnbull, *Acta Met.* 30 (1982) 2135.
- [35] G. Caginalp and E.A. Socolovsky, *Appl. Math. Lett.* 2 (1989) 117.
- [36] M.E. Glicksman, M.B. Koss and E.A. Winsa, *Phys. Rev. Lett.* 73 (1994) 573.
- [37] M.E. Glicksman, (1994), private communication.
- [38] X.W. Qian and H.Z. Cummins, *Phys. Rev. Lett.* 64 (1990) 3038.
- [39] L.M. Williams, M. Muschol, X. Qian, W. Losert and H.Z. Cummins, *Phys. Rev. E* 48 (1993) 489.
- [40] P. Bouissou, A. Chiffaudel, B. Perrin and P. Tabeling, *Europhys. Lett.* 13 (1990) 89.
- [41] M.N. Barber, A. Barbieri and J.S. Langer, *Phys. Rev. A* 36 (1987) 3340.